Title

A mechanistic model for creep lifetime of ferritic steels: Application to Grade 91

Permalink

Authors

Bieberdorf, Nathan
Tallman, Aaron
Kumar, M Arul
et al.

Publication Date

2021-12-01

DOI

10.1016/j.ijplas.2021.103086

Peer reviewed

A Mechanistic Model for Creep Lifetime of Ferritic Steels: Application to Grade 91

Nathan Bieberdorf[a,b], Aaron Tallman[a], M. Arul Kumar[a], Vincent Taupin[c], Ricardo A. Lebensohn[d] and Laurent Capolungo[a,*]

[a]*Materials Science and Technology Division, Los Alamos National Laboratory, Los Alamos, NM 87545, USA*

[b]*Department of Materials Science and Engineering, University of California, Berkeley*

[c]*Université de Lorraine, CNRS, Arts et Métiers ParisTech, LEM3, F-57000 Metz, France*

[d]*Theoretical Division, Los Alamos National Laboratory, Los Alamos, NM 87545, USA*

ARTICLE INFO

Keywords:
A. creep
B. crystal plasticity
B. viscoplastic material
B. porous material
C. finite elements

ABSTRACT

In this work, a physics-based crystal plasticity model is developed to predict failure in Grade 91 steel. A microstructure-sensitive dislocation kinetics law defines local plastic slip, an Arrhenius creep law is used to model vacancy-mediated plasticity, and strain hardening evolves with local dislocation density. As voids nucleate, a reaction-diffusion framework is adopted to dynamically track the local void size distributions, which grow by coupled viscoplastic and diffusive processes. Upon accurately reproducing the temperature and stress dependencies in primary, secondary, and tertiary creep seen experimentally for Grade 91 steel, the model is exercised to generate a material response database across a wide range of operating conditions. A new reduced-order lifetime predictor is developed from numerical predictions, and a Bayesian framework is used to quantify prediction uncertainties. When compared to current empirically-derived lifetime relations, the proposed lifetime assessment tool predicts rupture times up to several orders more conservative.

1. Introduction

For decades, high strength stainless steel have been key to maintaining the structural integrity and efficiency of power plants. In particular, steels alloyed with 9-12% chromium content have enabled operating temperatures greater than 600° C, and provide enhanced performance against oxidation and corrosion mechanisms (Abe, 2008; Cerri et al., 1998; Maruyama et al., 2001; Nakajima et al., 2003; Hald, 2008; Hayakawa et al., 2009). These alloys have also shown promising irradiation damage resistance, making them excellent candidates in nuclear energy applications, for example as fuel cladding in hot water reactors (Field et al., 2015; Yamamoto et al., 2015).

The use of these materials for industrial applications requires some *a priori* knowledge of their creep rupture life. This information is not rapidly accessible by experimentation and therefore not necessarily known when the lifespan of the system is expected to exceed several decades. Instead, accelerated creep tests are conducted at artificially elevated stresses and temperatures (Basirat et al., 2012; Shrestha et al., 2012), and empirical relations (e.g. Larson-Miller (Larson, 1952), Orr-Sherby-Dorn (Orr et al., 1953), Mendelson-Roberts-Manson (Mendelson et al., 1965)) are used to correlate the resultant short-term lifespans to more realistic long-term conditions. But as temperature and stress are lowered, a different set of deformation mechanisms are expected to drive the mechanical response, and empirical lifetime predictors provide no physical basis for extrapolating performance outside of the fitted deformation regime.

More recently, the Wilshire equations (Wilshire and Battenbough, 2007) introduced a bilinear fitting procedure and applied it to experimental creep data. The Wilshire equations use a power-law relation to model steady-state creep and vary the stress exponent to account for different deformation regimes above and below the yield stress. Creep lifetimes are then determined using the classical Monkman-Grant relationship (Monkman and Grant, 1956). (Whittaker and Harrison, 2014) enhanced the Wilshire equations by varying the activation energy for each deformation regime, and showed that several discontinuities in experimental creep data could be modeled. Using these equations, however, requires fitting experimental creep data at all intended operating conditions to determine the number and location of relevant deformation transitions.

---

*Corresponding author

✉ laurent@lanl.gov (L. Capolungo)

Ideally, extrapolation of a material's lifetime in untested conditions should rely on the use of mechanistic models that accurately quantify the roles of temperature and stress on the relative activation of dissipative processes. Several continuum damage models (CDM) for plasticity and damage in FeCr have been developed for Grade 91 steel (Gaffard et al., 2005; Basirat et al., 2012; Murchú et al., 2017) and have been shown to satisfactorily predict the creep response against experimental data. However, they do not address the correlation between the state of the microstructure and the material's performance. In practice, this can be achieved via the use and development of spatially resolved, microstructurally-sensitive mechanistic models.

The crystal plasticity (CP) formalism (Roters et al., 2010) can naturally be used to model the creep and creep damage in FeCr alloys. In terms of damage from nanoscale voids, polycrystal CP models usually rely on a homogenized description of damage within each material point. Locally-applied continuum damage mechanics (CDM) methods have been proposed within phenomenological CP models (Feng et al., 2002; Potirniche et al., 2007; Kim and Yoon, 2015), including a recent model for creep failure in FeCr alloys (Zhao et al., 2019). Mechanistic CP models are expected to be better suited for predicting creep and creep failure, as they track the coupled evolution of local internal variables, such as dislocation density, precipitate content, and void content. However, to date the authors are not aware of any mechanistic CP approaches to modeling both creep and creep damage in engineering alloys.

This work proposes a mechanistic CP constitutive law for thermal creep and failure in stainless steels. Further, a new approach is introduced to utilize these spatially resolved mechanistic models for deriving engineering scale creep rupture criteria. While the predictiveness of these rupture criteria is necessarily conditioned by that of the mechanistic model, one could utilize this type of approach to assess the creep resistance of metals for which limited data is available.

The crystal plasticity model by Wen et al. (Wen et al., 2017) is used to predict plastic strain mediated by dislocation motion. Vacancy-diffusion-mediated strain is accounted for using an Arrhenius creep rate law to model point defect migration along grain boundaries. While void nucleation is modeled using the well-known phenomenological law proposed by (Chu and Needleman, 1980), void growth is treated by utilizing a novel reaction-diffusion framework to dynamically track the evolution of pore size distribution within each material point. Void growth rates, based on coupled viscoplastic and diffusive processes, are computed using formulations by (Gurson, 1977; Needleman and Rice, 1980), and coalescence is modeled using the formulation by (Tvergaard and Needleman, 1984). The effect of porosity on local slip activity is correlated using the rate-sensitive, crystallographic homogenization law proposed by Mbiakop et al. (Mbiakop et al., 2015). The effect of porosity on local diffusion is correlated using the rate-sensitive isotropic homogenization law from Leblond et al. (Leblond et al., 1994).

The constitutive law is numerically implemented in an elasto-visco-plastic finite element framework to simulate thermal creep in a Grade 91 steel polycrystal, and the effects of stress and temperature on primary, secondary, and tertiary creep behavior seen experimentally (Basirat et al., 2012; Shrestha et al., 2012) are accurately captured. To the authors' knowledge, this is first time that physics-based descriptions of plasticity and damage have been combined in a full-field framework to predict transient creep response up to failure. In doing so, shortcomings and inconsistencies among these descriptions are identified to motivate future studies.

The model is then employed to generate a virtual database of material lifespan for varying thermomechanical boundary conditions beyond available experimental data. This database is used to derive a new reduced-order lifetime predictor for which a Bayesian uncertainty quantification framework is used to develop confidence intervals. This illustrates a potential path towards improving engineering standards for creep lifetime using predictive physics-based models. It is shown that at lower stresses and temperatures, the new lifetime relation predicts material lifespan several orders more conservative than empirical extensions of experimental data.

2. Model

Notation

Ψ — Local strain rate potential

$\Psi_{\text{dis}}, \Psi_{\text{dis}}^s$ Local strain rate potential for dislocation glide, slip rate potential for dislocation glide

Ψ_{diff} — Local strain rate potential for diffusion-mediated plasticity

$\dot{\boldsymbol{\varepsilon}}^p$ — Local strain rate tensor

$\dot{\boldsymbol{\varepsilon}}_{\text{dis}}^p, \dot{\boldsymbol{\varepsilon}}_{\text{diff}}^p$ Dislocation-controlled, diffusion-controlled strain rate tensors

$\boldsymbol{\sigma}, \boldsymbol{\sigma}'$ — Local stress tensor, deviatoric stress tensor

σ_{eq}, σ_m — Local von Mises equivalent stress, mean hydrostatic stress

$\tilde{\sigma}_{eq}$ — Local equivalent stress

$\bar{\dot{\gamma}}^s, \dot{\gamma}^s$ — Local, sub-material point slip-rate

$\tilde{\tau}^s, \tau^s$ — Local, sub-material point resolved shear stress

τ_c^s — Local critical resolved shear stress

s — Slip system

$\bar{f}, \bar{f}^*$ — Local mean porosity, adjusted for void coalescence

$\mathbf{m}^s$ — Schmid tensor

$\mathbf{b}^s, b^s$ — Burgers vector, magnitude

$\mathbf{n}^s$ — Slip plane normal vector

P — Probability distribution of sub-material point stresses

V_ρ — Variance in sub-material point stress distribution

$\rho_{\text{cell}}^s, \rho_{\text{cw}}^s$ Dislocation content within cells, at cell walls

v^s — Effective dislocation velocity

$t_{w,i}^s, t_{g,i}^s$ Dislocation waiting time, glide time at obstacle i, $i = \rho$ (other dislocations) and $i = \text{MX}$ (MX precipitates)

λ^s, λ_i^s Mean-free path between all slip obstacles, between i-type obstacles

$\alpha^{ss'}$ — Latent hardening coefficient between dislocations on slip-systems s and s'

ρ_0 — Mass density

E_Y, μ, ν Elastic modulus, shear modulus, Poisson's ratio

P_ρ — Proportion of dislocation-obstacle interactions that are dislocation-dislocation

$t_{g,i}, t_{c,i}$ Glide, climb duration for i-type obstacle interactions

R_e — Proportion of dislocations that are edge dislocations

v_c^s — Climb velocity

l_i — Climb distance to bypass i-type obstacles

D_v, D_{gb} Vacancy diffusivity in grains, at grain boundaries

$D_0, D_{gb,0}$ Diffusion constant within grains, at grain boundaries

E_m^v, E_f^v Vacancy migration energy within grains

$E_{gb,m}^v, E_{gb,f}^v$ Vacancy migration, formation energies at grain boundaries

S_f^v — Vacancy formation entropy

C_v^∞, C_v^0 Equilibrium, current (near-dislocation) vacancy concentrations

r_d, r_∞ Inner, outer radius of dislocation control volume

$\mathbf{f}_c, f_c^s$ Peach-Koehler force vector, climb component

$\mathbf{t}^s$ — Dislocation line tangent vector

Ω — Atomic volume

$v_{G,i}^s$ — Attempt frequency for dislocation-obstacle glide bypass

$\Delta G_i^s, \Delta G_{0,i}^s$ Activation energy for dislocation glide bypass, activation energy constant

p, q — Parameters for glide bypass activation energy

χ — Entropy factor

C_s — Shear wave velocity

τ_0^s — Friction shear stress

τ_ρ^s, τ_P^s Critical resolved shear stress from dislocation hardening, from precipitate hardening

m — Hardening exponent

$\dot{\rho}_{\text{cell}}^s, \dot{\rho}_{\text{cw}}^s$ Dislocation evolution within cells, at cell walls

$\dot{\rho}_{\text{cell,gen}}^s, \dot{\rho}_{\text{cell,ann}}^s, \dot{\rho}_{\text{cw,trap}}^s$ Dislocation evolution within cells due to generation, annihilation, and trapping at cell walls

$\dot{\rho}_{\text{cw,ann}}^s$ Dislocation evolution at cell walls due to annihilation

k_1, k_2, k_3, k_4 Dislocation evolution constants

$\dot{\varepsilon}_0, n_0$ Reference strain rate, exponent for dislocation annihilation within cells

λ_{sg} — Sub-grain size

A_a — Effective diffusion creep constant

E_a^v — Effective diffusion creep activation energy

$a, \bar{a}$ — Void radius, mean void radius

λ_f — Mean void spacing

$\tilde{n}_a$ — Number density of voids with radius a

$\tilde{n}_{\text{sat}}$ — Saturation number density of voids with radius a

$\tilde{n}_{a \to a^*}$ Number density of voids size a that evolve to size a^*

$\tilde{n}_{0 \to a}$ Number density of voids that nucleate with size a

f_a — Local porosity due to voids of size a

h — Geometric void-wetting shape factor

λ_f — Mean void spacing

F_ε — Strain-based void nucleation distribution

ε_c — Mean critical strain for void nucleation

V_ε — Variance in strain-based nucleation distribution

$\dot{a}^{vp}, \dot{a}^d$ Void growth due to viscoplasticity, diffusion

σ_s — Void sintering stress

γ_s — Void surface tension

σ_n — Local stress component normal to grain boundary

L — Characteristic vacancy-void diffusion distance

$\bar{f}_c, \bar{f}_s$ Critical, saturation porosity during coalescence

κ_c — Void coalescence factor

q_1, q_2 — Damage parameters

$\mathbf{S}^{var}, \mathbf{S}^{mvar}, \mathbf{S}$ Variational, modified variational, linear compliance tensors

$\mathbf{J}, \mathbf{K}, \mathbf{I}$ Hydrostatic, deviatoric, identity tensors

$\mathbf{M}^s$ — Schmid tensor

$\mathbf{Q}, \mathbf{S}^*$ Microstructure tensors

$\mathbf{P}$ — Eshelby tensor

q_J — Hydrostatic adjustment factor

$n_{\text{dis}}, n_{\text{diff}}$ Creep exponent for dislocation glide and diffusion-mediated plasticity

$\hat{\rho}, \hat{\kappa}$ Normalized modulus perpendicular to slip, normalized bulk modulus

Φ — Yield surface for Gurson-type gauge stress

H_n — Hydrostatic rate-sensitivity factor

2.1. Microstructure and Mechanisms Considered

Thermomechanical processing of Grade 91 steel yields a polycrystalline sample containing high initial dislocation content and a population of second phase particles that are located both in grain interiors and at grain boundaries. The presence of second phase particles increases the material's strength and also minimizes the contribution of grain boundary sliding (Sawada et al., 2005; Maruyama et al., 2001; Spigarelli et al., 1999; Kimura et al., 2013; Foldyna et al., 1996). Specifically, MX carbonitrides (M = V, Nb, and X = C, N) act as obstacles for dislocation motion within grains and sub-grains, while $M_{23}C_6$ carbides limit dislocation flow and annihilation within cell walls (sub-grain boundaries), thereby limiting sub-grain growth. Interaction between dislocations can also lead to latent hardening. Dislocations can bypass obstacles in the matrix by bowing around them via an Orowan glide process and by climb-assisted glide. Both processes are thermally-activated, and potentially simultaneous in creep conditions. Hardening will also evolve with dislocation content, which varies as dislocations generate, annihilate, and become trapped at cell walls (Basirat et al., 2012). At lower stresses, point-defect mediated mechanisms, such as dislocation climb and diffusion creep, become significant (Shrestha et al., 2013). In particular, at elevated temperatures common to thermal creep these diffusion processes will be localized to grain boundaries.

For complex alloys operating at high temperatures, dislocation glide and climb, and diffusional creep are the significant plastic deformation mechanisms (Ashby, 1983; Shrestha et al., 2013), and void nucleation, growth, and coalescence are the relevant damage processes (Besson, 2009; Gaffard et al., 2005). An overall plastic rate potential, Ψ, is defined to encode the stress-strain rate response by capturing the effects of microstructure and damage evolution. The overall rate potential may be approximated as the sum of rate potentials from each deformation mechanism (Wojtacki et al., 2020),

$$\Psi = \Psi_{\text{dis}} + \Psi_{\text{diff}} \tag{1}$$

where Ψ_{dis} and Ψ_{diff} are the local strain rate potentials for dislocation and vacancy diffusion processes, respectively. The local plastic strain rate tensor is the derivative of the plastic rate potential with respect to the local stress tensor:

$$\dot{\varepsilon}^p = \frac{\partial \Psi}{\partial \sigma} = \frac{\partial \Psi_{\text{dis}}}{\partial \sigma} + \frac{\partial \Psi_{\text{diff}}}{\partial \sigma} = \dot{\varepsilon}^p_{\text{dis}} + \dot{\varepsilon}^p_{\text{diff}} \tag{2}$$

where $\dot{\varepsilon}^p_{\text{dis}} = \partial \Psi_{\text{dis}}/\partial \sigma$ and $\dot{\varepsilon}^p_{\text{diff}} = \partial \Psi_{\text{diff}}/\partial \sigma$ are the local strain rate tensors due to dislocation motion and diffusional point defect transport, respectively.

2.2. Dislocation-Mediated Plasticity

Dislocation-controlled deformation is modeled using a crystal plasticity formulation for the plastic rate potential:

$$\Psi_{\text{dis}} = (1 - \bar{f}^*) \sum_s^K \Psi^s_{\text{dis}}(\tilde{\tau}^s) \tag{3}$$

where $\bar{f}^*$ is the local porosity, Ψ^s_{dis} is the slip-rate potential on each slip-system, s, K is the total number of slip systems, and $\tilde{\tau}^s$ is the local resolved shear stress, which is a function of the local stress tensor and porosity (i.e. $\tilde{\tau}^s = \tilde{\tau}^s(\sigma, \bar{f}^*)$). The local dislocation-controlled strain rate is therefore:

$$\dot{\varepsilon}^p_{\text{dis}} = \frac{\partial \Psi_{\text{dis}}}{\partial \sigma} = (1 - \bar{f}^*) \sum_s^K \bar{\gamma}^s(\tilde{\tau}^s) \frac{\partial \tilde{\tau}^s}{\partial \sigma} \tag{4}$$

where the local mean slip rate on each slip-system has been introduced, $\bar{\gamma}^s(\tilde{\tau}^s) = \partial \Psi^s_{\text{dis}}/\partial \tilde{\tau}^s$.

The local resolved shear stress is given by:

$$\tilde{\tau}^s(\sigma, \bar{f}^*) = \frac{\sqrt{\sigma : \mathbf{S}^{mvar} : \sigma}}{1 - \bar{f}^*} \tag{5}$$

where $\mathbf{S}^{mvar}$ is the modified variational compliance tensor, which is defined in Appendix A. In the limiting case of $\bar{f}^* = 0$, the resolved shear stress and derivative with respect to local stress become:

$$\tilde{\tau}^s(\sigma, 0) = \sigma : \mathbf{m}^s \tag{6}$$

$$\frac{\partial \tilde{\tau}^s(\sigma, 0)}{\partial \sigma} = \mathbf{m}^s = \frac{1}{2}\left(\mathbf{n}^s \otimes \mathbf{b}^s + \mathbf{b}^s \otimes \mathbf{n}^s\right) \tag{7}$$

where $\mathbf{m}^s$ is the deviatoric Schmid tensor, $\mathbf{b}^s$ is the Burgers vector and $\mathbf{n}^s$ is the unit vector normal to the slip plane.

The slip rate law from (Wen et al., 2017) is adopted here and described in the remainder of this subsection. Dislocation content is assumed to vary within each material point, leading to a locally heterogeneous resolved shear stress and slip rate. Following the approach by Wang et al.(Wang et al., 2016, 2017) , the mean local slip rate is modeled as an integral over slip rates from each sub-material point, within which dislocation content is relatively homogeneous:

$$\bar{\dot{\gamma}}^s(\tilde{\tau}^s) = \int_{-\infty}^{\infty} \dot{\gamma}^s(\tau^s) P(\tau^s - \tilde{\tau}^s) d\tau^s \tag{8}$$

where τ^s is the resolved shear stress at a sub-material point, $\dot{\gamma}^s$ is the corresponding slip rate, and P is a probability distribution function representing the volume fraction of each sub-material point. As an approximation, this volumetric weight function is modeled using a normal distribution of shear stresses about the mean value, $\tilde{\tau}^s$, with some variance, V_ρ, as follows:

$$P(\tau^s - \tilde{\tau}^s) = \frac{1}{\sqrt{2\pi V_\rho}} \exp\left(\frac{-(\tau^s - \tilde{\tau}^s)^2}{2V_\rho}\right) \tag{9}$$

Sub-material point slip rate is modeled from Orowan's equation:

$$\dot{\gamma}^s = \rho_{\text{cell}}^s b v^s \operatorname{sign}(\tau^s) \tag{10}$$

where ρ_{cell}^s is the current dislocation density within cells (sub-grains) on each slip system, v^s is the effective dislocation velocity, and b is the Burgers vector magnitude. The velocity of dislocations on a slip system depends on the mean-free path between obstacles, λ^s, and the total duration, t^s, a dislocation spends between them:

$$v^s = \frac{\lambda^s}{t^s} \tag{11}$$

The two obstacle types considered within grains are MX precipitates and other dislocations. Using a parallel circuit approximation, the effective mean spacing between obstacles is estimated as

$$\lambda^s = \left(\frac{1}{\lambda_{\text{MX}}^s} + \frac{1}{\lambda_{\rho,\text{cell}}^s}\right)^{-1} \tag{12}$$

where λ_{MX}^s and $\lambda_{\rho,\text{cell}}^s$ are the mean-free path between MX precipitates and between dislocations within cells, respectively. Dislocation mean free path evolves with local content (Franciosi and Zaoui, 1982; Bertin et al., 2014):

$$\frac{1}{\lambda_{\rho,\text{cell}}^s} = \sqrt{\sum_s^K \alpha^{ss'} \rho_{\text{cell}}^{s'}} \tag{13}$$

where $\alpha^{ss'}$ is the effective latent hardening matrix, which varies depending on whether dislocations are coplanar $(s = s')$.

The time a dislocation spends traveling between obstacles, t^s, is the sum of the waiting time and travel time (Lloyd et al., 2014; Clifton, 1971; Austin and McDowell, 2011):

$$t^s = t_w^s + t_t^s \tag{14}$$

The travel time is negligible compared to the waiting time, and may be approximated by assuming that dislocations move by the shear wave velocity, $t_t^s = \lambda^s / C_s$ (Kocks et al., 1975), where $C_s = \sqrt{\mu/\rho_0}$ is the shear wave velocity, and ρ_0 and μ are the mass density and shear modulus, respectively.

The waiting time will vary depending on the type of obstacle encountered, and therefore depends on the probability of encountering either an MX precipitate or another dislocation:

$$t_w^s = P_\rho t_{w,\rho}^s + (1 - P_\rho)t_{w,\text{MX}}^s \tag{15}$$

where $t_{w,\rho}^s$ and $t_{w,\text{MX}}^s$ are the waiting times associated with dislocation and MX precipitate interaction, respectively, and P_ρ is the probability of encountering another dislocation, which is given by the ratio of dislocation spacing to overall obstacle spacing:

$$P_\rho = \frac{1/\lambda_\rho^s}{1/\lambda^s} \tag{16}$$

In this work, dislocations are assumed to bypass obstacles by two simultaneous processes, thermally-activated glide and diffusion-assisted climb, with waiting times $t_{g,i}$ and $t_{c,i}$ respectively:

$$t_{w,i} = \left(\frac{1}{t_{g,i}} + \frac{1}{t_{c,i}} \right)^{-1} \tag{17}$$

where i denotes the obstacle type ($i = \rho, \text{MX}$ for dislocations, MX precipitates, respectively).

The waiting time associated with climb is given by (Patra and McDowell, 2012):

$$\frac{1}{t_{c,i}} = R_e \frac{|v_c^s|}{l_i} \tag{18}$$

where R_e is the proportion of dislocations which are edge dislocations (since only these may climb), v_c^s is the climb velocity of edge dislocations, and l_i is the average climb distance required to bypass an obstacle. The climb velocity may be determined from the vacancy current in the dislocation control volume (Was, 2016; Hirth et al., 1983; Geers et al., 2014; Bakó et al., 2011; Gu et al., 2015):

$$v_c^s = \frac{2\pi D_v \left[C_v^\infty - C_v^0 \exp\left\{ \left(\frac{-f_c^s \Omega}{kTb} \right) \right\} \right]}{b \ln (r_\infty/r_d)} \tag{19}$$

where D_v is the vacancy diffusivity within grains, C_v^∞ is the equilibrium vacancy concentration of the material, C_v^0 is the current vacancy concentration (which is assumed equal to C_v^∞ in the model), f_c^s is the climb component of the Peach-Koehler force, r_d and r_∞ denote the inner and outer radii of the cylindrical control volume, Ω is the atomic volume, k is the Boltzmann constant, and T is the applied temperature. In the dislocation control volume definition, r_d represents the dislocation core radius, and between r_d and r_∞ a vacancy concentration gradient develops leading to a flux of vacancies towards or away from the dislocation line. For a detailed derivation of this vacancy climb velocity, the reader is directed to the Appendix of (Wen et al., 2017).

The climb component of the Peach-Koehler force is obtained by projecting the Peach-Koehler force along the slip plane normal:

$$f_c^s = \mathbf{f}_c \cdot \mathbf{n}^s \tag{20}$$

and the Peach-Koehler force is as follows (Hartley, 2003; Lebensohn et al., 2010):

$$\mathbf{f}_c = \left[(\sigma' \cdot \mathbf{b}^s) \times \mathbf{t}^s \right] \tag{21}$$

where σ' is the deviatoric stress tensor at a material point, and $\mathbf{t}^s$ is the unit tangent vector to the dislocation line: $\mathbf{t}^s = \mathbf{n}^s \times \mathbf{b}^s$.

The equilibrium vacancy concentration is given by (Was, 2016):

$$C_v^0 = \exp\left(\frac{S_f^v}{k} \right) \exp\left(-\frac{E_f^v}{kT} \right) \tag{22}$$

where S_f^v and E_f^v are the vacancy formation entropy and energy, respectively. Vacancy diffusivity is calculated as:

$$D_v = D_0 \exp\left(-\frac{E_m^v}{kT}\right) \tag{23}$$

where D_0 is a pre-factor and E_m^v is the energy barrier for vacancy diffusion, i.e. vacancy migration energy.

The waiting time associated with dislocation glide-bypass of obstacle-type i is given by (Lloyd et al., 2014; Austin and McDowell, 2011; Kocks et al., 1975):

$$\frac{1}{t_{g,i}} = v_{G,i}^s \exp\left(\frac{\Delta G_i^s}{kT}\right) \tag{24}$$

where $v_{G,i}^s$ is the effective attempt frequency, and ΔG_i^s is the activation energy given by:

$$\Delta G_i^s = \begin{cases} \Delta G_{0,i} \left(1 - \left(\frac{\tau^s}{\tau_c^s}\right)^p\right)^q, & \text{if } \tau^s < \tau_c^s \\ 0, & \text{if } \tau^s \geq \tau_c^s \end{cases} \tag{25}$$

In the above, $\Delta G_{0,i}$ is the activation energy in the absence of any applied stress, τ_c^s is the critical resolved shear stress, and p and q are terms describing the shape of the obstacles resistance profile (Kocks et al., 1975).

The effective attempt frequency for overcoming MX precipitates is assumed constant, while for overcoming dislocations it can be described as (Wen et al., 2017; Wang et al., 2017)

$$v_{G,\rho} = \chi C_s / \lambda^s \tag{26}$$

where χ is the entropy factor, which encodes the temperature-independent entropy of activation for dislocation-glide bypass (Granato et al., 1964).

The critical resolved shear stress on each slip system evolves with latent hardening due to dislocation and precipitate content, which may be added in superposition (Sobie et al., 2015; Dong et al., 2010; Lagerpusch et al., 2000):

$$\tau_c^s = \tau_0^s + \left(\left(\tau_\rho^s\right)^m + \left(\tau_P^s\right)^m\right)^{1/m} \tag{27}$$

where the frictional stress, τ_0^s, must be added linearly to the harmonic mean of dislocation hardening τ_ρ^s and precipitate hardening τ_P^s, with factor m. Hardening due to both MX and $M_{23}C_6$ precipitates are combined in the τ_P^s term above and vary with temperature. Latent hardening on each slip system due to dislocation content within cells, ρ_{cell}^s, and at cell walls, ρ_{cw}^s, is given by:

$$\tau_\rho^s = \mu b \sqrt{\sum_s^K \alpha^{ss'} \left(\rho_{\text{cell}}^{s'} + \rho_{\text{cw}}^{s'}\right)} \tag{28}$$

The evolution of dislocation content is based on dislocation generation, $\dot{\rho}_{\text{cell,gen}}^s$, annihilation, $\dot{\rho}_{\text{cell,ann}}^s$, and trapping at cell walls, $\dot{\rho}_{\text{cw,trap}}$:

$$\dot{\rho}_{\text{cell}}^s = \dot{\rho}_{\text{cell,gen}}^s - \dot{\rho}_{\text{cell,ann}}^s - \dot{\rho}_{\text{cw,trap}}^s \tag{29}$$

The dislocation generation rate is given by:

$$\dot{\rho}_{\text{cell,gen}}^s = \frac{k_1}{b \lambda^s} |\dot{\bar{\gamma}}^s| \tag{30}$$

Dislocation annihilation is modeled using the Kocks-Mecking law, with strain-rate dependent recovery parameters from (Estrin, 1998):

$$\dot{\rho}_{\text{cell,ann}}^s = k_2 \left(\frac{\dot{\epsilon}_0}{\dot{\epsilon}_{eq}}\right)^{\frac{1}{n_0}} \rho_{\text{cell}}^s |\dot{\bar{\gamma}}^s| \tag{31}$$

where $\dot{\varepsilon}_0$ and n_0 are temperature-dependent parameters but in the current work are approximated to be constant across the narrow temperature range considered. Dislocations are assumed to arrest at sub-grain boundaries, and therefore the trapping rate is inversely related to the sub-grain size, λ_{sg}:

$$\dot{\rho}_{cw,trap}^{s} = \frac{k_3}{\lambda_{sg}}|\bar{\dot{\gamma}}^s| \tag{32}$$

Dislocation density evolution within cell walls is given by:

$$\dot{\rho}_{cw}^{s} = \dot{\rho}_{cw,trap}^{s} - \dot{\rho}_{cw,ann}^{s} \tag{33}$$

Dislocations within cell walls may only move and annihilate by climb. The climb-annihilation rate may be considered proportional to climb velocity and dislocation density raised to the power 3/2 (Nes, 1997; Wen et al., 2017):

$$\dot{\rho}_{cw,ann}^{s} = k_4 |v_c^s| \left(\rho_{cw}^s\right)^{\frac{3}{2}} \tag{34}$$

In Eqs 30, 31, 32, and 34, k_1, k_2, k_3, and k_4 are proportionality constants.

2.3. Diffusion-Mediated Plasticity

At elevated temperatures, point-defect-mediated straining mechanisms are assumed present. As stresses are reduced and dislocations become less mobile, these point-defect transport mechanisms will start to dominate overall plastic response (Ashby, 1983). The present work models diffusion-controlled plasticity using a rate potential that is a function of the isotropic equivalent stress:

$$\Psi_{diff} = \Psi_{diff}(\tilde{\sigma}_{eq}) \tag{35}$$

where $\tilde{\sigma}_{eq} = \tilde{\sigma}_{eq}(\sigma, \bar{f}^*)$. The diffusion-controlled strain rate is therefore:

$$\dot{\varepsilon}_{diff}^{p} = \frac{\partial \Psi_{diff}}{\partial \sigma} = \frac{A_a}{T} \exp\left(\frac{-E_a^v}{kT}\right) \tilde{\sigma}_{eq} \frac{\partial \tilde{\sigma}_{eq}}{\partial \sigma} \tag{36}$$

where

$$\frac{A_a}{T} \exp\left(\frac{-E_a^v}{kT}\right) \tilde{\sigma}_{eq} = \frac{\partial \Psi_{diff}}{\partial \tilde{\sigma}_{eq}} \tag{37}$$

has been defined, with A_a as an effective creep constant and E_a^v as the effective energetic barrier for all point-defect diffusive processes, following (Wen et al., 2020). In this work, diffusive processes are assumed to be active within grains and at grain boundaries, and so Eq. 36 is active at each material point. The equivalent stress is fully defined in Appendix B, but in the absence of damage,

$$\tilde{\sigma}_{eq}(\sigma, 0) \cdot \frac{\partial \tilde{\sigma}_{eq}}{\partial \sigma}(\sigma, 0) = \sigma' \tag{38}$$

2.4. Void Evolution
2.4.1. Local Void Distributions

A reaction-rate framework is proposed to track the distribution of porosity size and spacing within each material point. This allows for modeling the continuous nucleation and growth of voids, without necessarily modeling them discretely. The number density $\tilde{n}_a$ of voids with size a, will change by the number density, $\tilde{n}_{a^* \to a}$, of voids that evolve (grow or shrink) to that size from any other size a^*, minus the number density of voids which evolve from that size, plus the number density, $\tilde{n}_{0 \to a}$, of voids which have nucleated with size a:

$$\Delta \tilde{n}_a = \sum_{a^*} \left\{ \tilde{n}_{a^* \to a} - \tilde{n}_{a \to a^*} \right\} + \tilde{n}_{0 \to a} \tag{39}$$

with:

$$\tilde{n}_{a \to a^*} = \begin{cases} \tilde{n}_a, & \text{if } a + \dot{a}\Delta t = a^* \\ 0, & \text{otherwise} \end{cases} \tag{40}$$

Void generation is similarly given by,

$$\tilde{n}_{0 \to a} = \begin{cases} \tilde{n}_0, & \text{if } a_0 = a \\ 0, & \text{otherwise} \end{cases} \tag{41}$$

where voids are assumed to nucleate at a stable radius, a_0, that balances applied load and void surface tension (see Eqs 51, 54, and 55).

The volumetric porosity, f_a, for each population of voids with size a, is computed from their void radius and number density,

$$f_a = h(\theta) a^3 \tilde{n}_a \tag{42}$$

where $h(\theta)$ is a geometric factor to account for the wetting angle, θ, in porosity calculation, given by (Chuang et al., 1979).:

$$h(\theta) = \frac{(1 + \cos\theta)^{-1} - \frac{1}{2}\cos\theta}{\sin\theta} \tag{43}$$

Mean spacing, λ_f, at each material point is given by:

$$\lambda_f = \left(\sum_a \tilde{n}_a^{1/3} \right)^{-1} \tag{44}$$

and mean porosity at each material point is simply the sum of the local porosity distribution,

$$\bar{f} = \sum_a f_a \tag{45}$$

Mean void size, $\bar{a}$, within each material point is approximated using,

$$\bar{a} = \lambda_f \left(\frac{\bar{f}}{h(\theta)} \right)^{\frac{1}{3}} \tag{46}$$

The evolution of each population should still reflect the presence of other voids within the same material point. For this reason, these mean magnitudes for void size and spacing are used to describe local void evolution in the following subsections.

2.4.2. Void Nucleation

Recent molecular dynamics simulations have shown that void nucleation is a strain-controlled process (Sills and Boyce, 2020). However, the specific process is not well-understood, so in the current work the criterion from Chu and Needlemen is used, which assumes that voids nucleate by a distribution of local strain:

$$\dot{\tilde{n}}_{0 \to a} = F_\varepsilon(\varepsilon^p) \dot{\varepsilon}^p_{eq} \tag{47}$$

with,

$$F_\varepsilon(\varepsilon^p) = \frac{\tilde{n}_{\text{sat}}}{\sqrt{2\pi V_\varepsilon}} \exp\left(\frac{-(\varepsilon^p_{eq} - \varepsilon_c)^2}{2 V_\varepsilon} \right) \tag{48}$$

In the above $\tilde{n}_{\text{sat}}$ is the saturation number density of voids, ε_c is the mean critical magnitude for nucleation strain, and V_ε is the statistical variance in critical nucleation strain and stress. The local strain state is quantified in the above by equivalent von-Mises plastic strain, ε^p_{eq}.

Experimentally, cavitation has been seen preferential to locations along the grain boundary (Shrestha et al., 2012; Pandey et al., 2018). Therefore, the current work limits void nucleation to only those material points which lie along grain boundaries.

2.4.3. Void Growth

The viscoplastic and diffusive creep processes will simultaneously grow voids, and, following (Van Der Giessen et al., 1995; Sham and Needleman, 1983), each process is considered additive in the current work:

$$\dot{a} = \dot{a}^{vp} + \dot{a}^{d} \tag{49}$$

where, $\dot{a}^{vp}$ and $\dot{a}^{d}$ are growth rates due to local viscoplasticity and viscoplastic-assisted diffusion, respectively.

Viscoplastic void growth can be quantified by the hydrostatic strain in each material point (Gurson, 1977):

$$\dot{a}^{vp} = \frac{\lambda_f^3}{3\bar{a}^2 h(\theta)} \left(1 - \bar{f}\right) \mathrm{tr}(\dot{\varepsilon}_{\mathrm{dis}}^{p}) \tag{50}$$

The diffusive void growth arises from the increased point defect flux along grain boundaries, and the expressions from Needleman and Rice (Needleman and Rice, 1980) are used in this work and recounted below:

$$\dot{a}^{d} = \frac{D}{\bar{a}^2 h(\theta)} \frac{\sigma_n - (1 - f_{\mathrm{adj}})\sigma_s}{\ln\left(\frac{1}{f_{\mathrm{adj}}}\right) - \frac{1}{2}(3 - f_{\mathrm{adj}})(1 - f_{\mathrm{adj}})} \tag{51}$$

In the above, σ_n is the stress resolved in the grain boundary normal direction, and D is a term for describing diffusion along grain boundaries,

$$D = \frac{D_{gb}\delta_{gb}\Omega}{kT} \exp\left(-\frac{E_{gb,f}^{v}}{kT}\right) \tag{52}$$

D_{gb} is the vacancy diffusion coefficient along grain boundaries, and δ_{gb} is the thickness of heightened diffusivity centered along grain boundaries. Vacancy diffusion along grain boundaries is given by:

$$D_{gb} = D_{gb,0} \exp\left(-\frac{E_{gb,m}^{v}}{kT}\right) \tag{53}$$

where $D_{gb,0}$ is the grain boundary diffusion pre-factor. In the above equations, $E_{gb,f}^{v}$ and $E_{gb,m}^{v}$ are the vacancy formation and migration energies, respectively, at grain boundaries.

The sintering stress, σ_s, gives an effective surface tension for the void based on the free surface energy of the material, γ_s, and the void's geometry:

$$\sigma_s(a) = \frac{2\gamma_s \sin\theta}{a} \tag{54}$$

Sintering will occur if the surface tension of the void is greater than the applied force (i.e. when the numerator of Eq 51 is less than zero). This can be used to imply a critical void radius, a_0

$$a_0 = \frac{2\gamma_s \sin\theta}{\sigma_n} \tag{55}$$

above which voids will be considered stable and growing. This critical void size is assigned to populations which nucleate according to Eq 47.

(Needleman and Rice, 1980) account for viscoplastic creep-assisted diffusion by the adjusting the porosity term in Eq 51:

$$f_{\mathrm{adj}} = \max\left\{ \left(\frac{\bar{a}}{\lambda_f}\right)^2, \left(\frac{\bar{a}}{\bar{a} + 1.5L}\right)^2 \right\} \tag{56}$$

where the second term becomes larger when plastic deformation near the void reduces the characteristic length, L, along which vacancies diffuse:

$$L = \left(\frac{D\sigma_{eq}}{\dot{\varepsilon}_{eq}^{p}}\right)^{1/3} \tag{57}$$

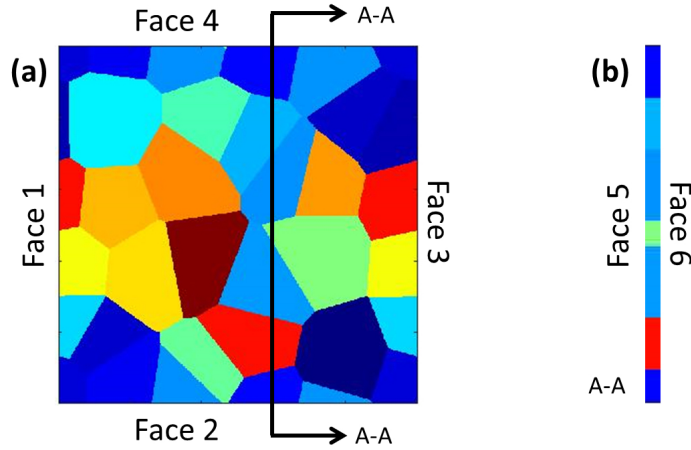giving rise to growth rates several orders greater than in the rigid-grain formulations by (Hull and Rimmer, 1959).

Figure 1: (a) Front view and (b) side view of polycrystalline structure randomly generated using a Voronoi tesselation procedure

2.4.4. Void Coalescence

The coalescence of spherical voids leads to elongated-shape and orientation effects, which are empirically captured in the current work using the criteria of (Tvergaard and Needleman, 1984):

$$
\bar{f}^* = \begin{cases} \bar{f}, & \text{if } \bar{f} \leq \bar{f}_c \\ \bar{f}_c + \kappa_c(\bar{f} - \bar{f}_c), & \text{if } \bar{f} > \bar{f}_c \end{cases} \tag{58}
$$

where $\bar{f}_c$ is the critical porosity above which coalescence occurs in a material point, and κ_c is a coalescence factor:

$$
\kappa_c = \frac{1/q_1 - \bar{f}_c}{\bar{f}_s - \bar{f}_c} \tag{59}
$$

where $\bar{f}_s$ is the saturation porosity of each material point.

2.5. Finite Element Model

The entire constitutive law is implemented in an elasto-visco-plastic finite element framework, with elastic modulus $E_Y = 2\mu(1 + \nu)$ and Poisson's ratio ν. The open-source finite element solver FreeFEM++ (Hecht, 2012) is used to represent a thin plate that comprises a 5x5 grain structure. The plate is discretized using a 49x49x2 volume of tetrahedral elements, with quadratic interpolation between nodes. This mesh density was seen to be convergent relative to higher density meshes. The modeled polycrystal is shown in Figure 1.

Eighth-symmetry in the model is enforced by fixing displacements to zero in the horizontal, vertical, and out-of-plane directions on faces 1, 2, and 5 respectively. Positive stress is applied normal to face 3 and held constant over time to simulate uniaxial tensile creep.

3. Results

3.1. Parameterization

The crystal plasticity model was originally implemented and calibrated by (Wen et al., 2017) in the mean-field viscoplastic self-consistent (VPSC) framework (Lebensohn and Tomé, 1993). The current work is calibrated using the same experimental dataset for Grade 91 steel (Shrestha et al., 2012; Basirat et al., 2012), however several parameters are changed to improve the fit. The variance, V_ρ, in the sub-material stress distribution (Eq. 9) was reduced by 10% to limit constructive interference between finite element nodes. The precipitate hardening, τ_{MX}, was varied slightly to improve fits to steady-state creep rate. To improve stress-sensitivity of the model, parameters controlling the climb-assisted glide of dislocations around obstacles were adjusted. First, the climb-distance for dislocations to bypass other

dislocations, l_ρ, was lowered to a more realistic value. Then, l_ρ and l_{MX} were slightly increased to account for the kinetics of transition between climb and glide processes. The inner radius of the dislocation control volume, r_d, was also lowered by a factor 2 with this in mind.

The diffusion-mediated plasticity law is calibrated based on steady-state creep rates, particularly at lower stresses and higher temperatures. The activation energy for diffusion creep is assumed to be the sum of vacancy formation and migration energies, $E_a^v = E_f^v + E_a^v$. In the temperature range considered, this gives $E_a^v \approx 2.43$ eV, which is similar to the activation energy measured for diffusion creep in the experimental validation set (Shrestha et al., 2013). Rather than explicitly defining a dependence on grain size, an effective creep constant A_a was chosen, following (Wen et al., 2020). It is noted that smaller grains should increase this creep constant to increase the diffusion-mediated strains.

The nucleation rate law was calibrated against the tertiary creep response measured in (Shrestha et al., 2012; Basirat et al., 2012). The total number density of potential nucleation sites per unit volume is 1×10^{22} m^{-3}, and the void nucleation distribution has a variance of 0.02 about a mean of 0.08.

The grain boundary thickness is taken as 0.7 nm, and surface energy is assumed 1 J/m^2 for Grade 91 steel, which gives a stable void radius between 5-70 nm depending on the applied loads. Vacancy formation and migration energies are assumed to be lower at grain boundaries than within grains, so their sum at grain boundaries is defined to be 1.8 eV. To obtain the best match to experimental data, the grain boundary diffusion pre-factor in Eq. 52 was used as a fitting parameter for the diffusion void growth law, and is significantly lower than for within grains, which was required to maintain realistic void growth rates.

It is assumed that void shape is controlled by growth kinetics. In the current work, voids maintain quasi-spherically shape under diffusion and viscoplastic deformation, and a representative wetting angle of $\theta = 70°$ is selected following (Needleman and Rice, 1980). A smaller angle could be used to imply a larger ratio of diffusive growth along grain boundaries, while $\theta = 90°$ would represent perfectly spherical voids.

Coalescence is assumed to occur once porosity reaches $\bar{f}_c = 0.1$, and local porosity saturation occurs at $\bar{f}_s = 0.3$, which are within typical ranges (Gaffard et al., 2005; Gurson, 1977; Tvergaard and Needleman, 1984).

The modified compliance tensor for dislocation-controlled strain (used in Eq. 5 and defined in Appendix A) was originally developed by (Mbiakop et al., 2015) using a Norton power law for creep and therefore requires selection of a stress exponent. In the present work, a stress exponent $n_{dis} = 10$ is chosen to match the strain-rate sensitivity seen experimentally for this material system (Shrestha et al., 2013), but it should be noted that different selections of the stress exponent were seen to have minimal effect on overall creep response. Similarly, to compute the equivalent stress for diffusion-controlled plasticity, a stress exponent $n_{diff} = 1$ was used based on the linear form of Eq. 36.

The predictive capability of the model could have been enhanced by fitting to replicate creep experiments. However, creep experiments repeated at the same temperature and stress were not published by (Shrestha et al., 2012; Basirat et al., 2012). Creep experiments from other experimental sources are available, but it was assumed that their inclusion would have introduced additional sources of uncertainty.

Parameters for the entire constitutive law are given in Table 1.

Table 1
Parameters used for Fe-Cr-Mo (Grade 91) steel in this work.

ine Parameter		Reference
ine b	2.48×10^{-10} m	(Wen et al., 2017)
V_ρ	900 MPa^2	adjusted from (Wen et al., 2017)
λ^s_{MX}	3×10^{-7} m	(Wen et al., 2017)
$\alpha^{ss'}$	0.7 ($s = s'$), 0.05 ($s \neq s'$)	(Queyreau et al., 2009)
τ_P	310 MPa (973 K),	adjusted from (Wen et al., 2017)
	332 MPa (923 K),	
	370 MPa (873 K)	
m	2	(Sobie et al., 2015; Dong et al., 2010; Lagerpusch et al., 2000)
ρ_0	8000 kg/m^3	(Wen et al., 2017)
μ	103572 MPa $- T \cdot 48$ MPa/K	(Gaffard, 2004)
ν	0.33	
R_e	10%	(Wen et al., 2017)
l_ρ	$5b$	adjusted from (Wen et al., 2017)
l_{MX}	4.63×10^{-8} m	adjusted from (Wen et al., 2017)
D_0	7.87×10^{-7} m^2/s	(Mendelev and Mishin, 2009)
E^v_f	$g_0 - g_2 T^2 - 2g_3 T^3$ eV	(Mendelev and Mishin, 2009)
E^v_m	0.6 eV	(Mendelev and Mishin, 2009)
S^v_f	$-g_1 - 2g_2 T - 3g_3 T^2$ eV	(Mendelev and Mishin, 2009)
g_0	1.724 eV	(Mendelev and Mishin, 2009)
g_1	-1.2×10^{-4} eV/K	(Mendelev and Mishin, 2009)
g_2	-2.79×10^{-8} eV/K^2	(Mendelev and Mishin, 2009)
g_3	-5.93×10^{-11} eV/K^3	(Mendelev and Mishin, 2009)
r_d, r_∞	$2b$, $200b$	adjusted from (Wen et al., 2017)
χ	1	(Wang et al., 2017)
$\upsilon_{G,\text{MX}}$	1.2×10^{-1} s^{-1}	(Patra and McDowell, 2012)
$\Delta G_{0,\rho}$	2.7 eV	(Wen et al., 2017)
$\Delta G_{0,\text{MX}}$	7 eV	(Wen et al., 2017)
p, q	0.7, 1.4	(Kocks et al., 1975)
$\rho^s_{cell,0}$	4×10^{12} m^{-2}	(Yadav et al., 2016)
$\rho^s_{cw,0}$	1×10^{13} m^{-2}	(Yadav et al., 2016)
k_1	0.12	(Wen et al., 2017)
k_2	85	(Wen et al., 2017)
k_3	5×10^8	(Wen et al., 2017)
k_4	0.1	(Wen et al., 2017)
n_0	3.5	(Wen et al., 2017)
$\dot{\varepsilon}_0$	1 s^{-1}	(Wen et al., 2017)
A_a	1.1×10^4 MPa^{-1}s^{-1}	
E^v_a	$E^f_m + E^v_m$	(Shrestha et al., 2013)
n_{dis}	10	(Shrestha et al., 2013)
n_{diff}	1	(Shrestha et al., 2013)
q_1, q_2	1.5, 1.0	(Tvergaard and Needleman, 1984)
$\tilde{n}_{\text{sat}}$	1×10^{22} m^{-3}	
V_ε	0.02	
$\bar{\varepsilon}_c$	0.08	
$D_{gb,0}$	1.48×10^{-8} m^2/s	
$E^v_{gb,f} + E^v_{gb,m}$	1.8 eV	
δ_{gb}	0.7 nm	
γ_s	1 J/m^2	
$\bar{f}_c$	0.1	
$\bar{f}_f$	0.3	
ine		

3.2. Creep Simulations

Numerical creep results are validated against short-term experimental data for Grade 91 steel from (Shrestha et al., 2012; Basirat et al., 2012) at temperature 873 K with applied uniaxial stresses 100, 150, 200, and 225 MPa, at 923 K with 100 and 150 MPa, and at 973K with 80, 100, and 150 MPa. Numerical and experimental data are shown in Figures 2-4 for creep and creep rate. Note that in (Shrestha et al., 2012; Basirat et al., 2012), creep strain was not published for 873 K 100 MPa and 923 K 100 MPa, and creep tests were interrupted prior to rupture for 873 K 100 MPa and 873 K 150 MPa experiments.

Across the experimental loading conditions, the constitutive law captures the primary, secondary, and tertiary creep response. Specifically, the model is able to predict the sensitivity of secondary (steady-state) creep rate to the loading conditions. Indeed, small changes in applied stress or temperature can vary the steady-state creep rate by several orders of magnitude, and this is quantitatively captured by the proposed model. Further, with the newly-proposed damage model, the onset of tertiary creep regime up to failure is predicted. The transition between secondary and tertiary creep is very abrupt at high stresses, leading to a relatively short-lived steady-state regime before failure, while at lower stresses this transition is more gradual. These subtleties, which are controlled by temperature- and stress-dependent deformation and void growth processes, are captured by the model.

Interestingly, with the parameters in Table 1, the model was unable to predict failure in the highest temperature, highest stress experiments from (Shrestha et al., 2012; Basirat et al., 2012) (200 MPa at 923 K and 973 K, not shown here). Rather than entering the tertiary creep regime, the material maintained its steady-state creep rate for an indefinite amount of time (until the simulation was manually terminated). By restarting the simulations with a higher saturation porosity ($\bar{f}_s = 0.5$), failure was seen to occur at times similar to experiment, which suggests a need to vary the damage law for these thermomechanical conditions. However, the current work focuses on quantifying long-term creep behavior, and the creep rupture times from these experiments are only 30 and 3 minutes for 200 MPa at 923 K and 973 K, respectively. Therefore, they are simply not included in the calibration set. Additionally, the experimental primary creep regime trends are not quantitatively captured by the numerical model. These regimes are also very short-lived, and so, in this work, primary creep accuracy is not considered essential to predicting steady-state creep rates and rupture lifetimes.

3.3. Lifetime Assessment Tool

The CP model is exercised to generate a large virtual database of creep tests ranging from 30 to 225 MPa in applied stress and 873 to 973 K in temperature. The genetic programming module GP-Learn (Stephens, 2019) is trained against the entire database of experimental and numerical creep tests to determine a closed form, reduced-order lifetime relation as a function of applied stress and temperature. When developing the new lifetime relation, many functional forms were explored before concluding that the most accurate fit came from mapping a polynomial function of inverse temperature and the logarithm of applied stress to the logarithm of resultant rupture time. In the present work, rupture time is measured when the material creeps at a rate 10% above its steady-state creep rate. The lifetime relation developed herein is given by the following equation:

$$
\log_{10}(t_r) = \alpha_\Sigma \log_{10}(\Sigma) + \alpha_{\Sigma^5} \log_{10}(\Sigma)^5 + \frac{1}{T}\left(\alpha_T + \alpha_{T\Sigma} \log_{10}(\Sigma) + \alpha_{T\Sigma^2} \log_{10}(\Sigma)^2\right)
$$
$$
+ \frac{1}{T^2}\left(\alpha_{T^2\Sigma} \log_{10}(\Sigma) + \alpha_{T^2\Sigma^2} \log_{10}(\Sigma)^2\right) + \frac{1}{T^3}\left(\alpha_{T^3\Sigma} \log_{10}(\Sigma) + \alpha_{T^3\Sigma^2} \log_{10}(\Sigma)^2\right) \tag{60}
$$
$$
+ \frac{1}{T^4}\left(\alpha_{T^4\Sigma^2} \log_{10}(\Sigma)^2\right) + \alpha_0
$$

where Σ is the uniaxial applied stress and the coefficients are:

$$
\begin{aligned}
&\alpha_\Sigma = 4.69 \times 10^7, && \alpha_{\Sigma^5} = -2.69 \times 10^{-1}, && \alpha_T = 9.19 \times 10^3, && \alpha_{T\Sigma} = -1.30 \times 10^{11}, \\
&\alpha_{T\Sigma^2} = 4.94 \times 10^4, && \alpha_{T^2\Sigma} = 1.20 \times 10^{14}, && \alpha_{T^2\Sigma^2} = -6.28 \times 10^7, && \alpha_{T^3\Sigma} = -3.68 \times 10^{16}, \\
&\alpha_{T^3\Sigma^2} = 1.31 \times 10^{10}, && \alpha_{T^4\Sigma^2} = 1.02 \times 10^{13}, && \alpha_0 = 1.24 \times 10^1,
\end{aligned}
$$

The proposed creep rupture life model can be compared to more traditional methods of lifetime prediction. Typically, short-term experimental data is fit to an empirical relation that is used to extrapolate towards lower stresses. A common empirical lifetime relation is the Larson-Miller equation (Larson, 1952):

$$
\log_{10}(t_r) = \frac{1}{T}\left(\alpha_T + \alpha_{T\Sigma} \log_{10}(\Sigma) + \ldots + \alpha_{T\Sigma^n} \log_{10}(\Sigma)^n\right) - \alpha_0 \tag{61}
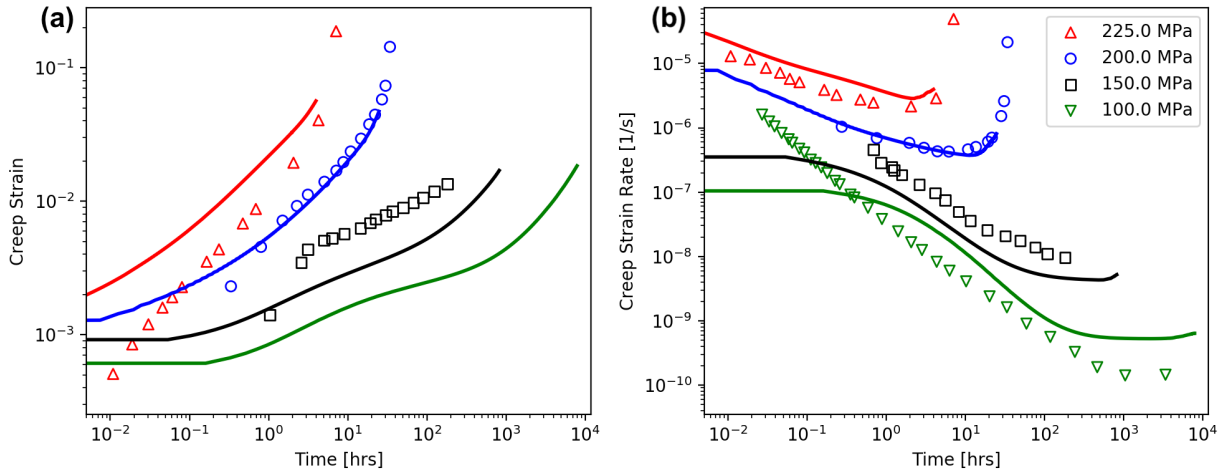$$

Figure 2: (a) Creep strain and (b) Creep rate for 873 K, open symbols represent the experimental data from (Shrestha et al., 2012; Basirat et al., 2012) and solid lines are from the numerical model.
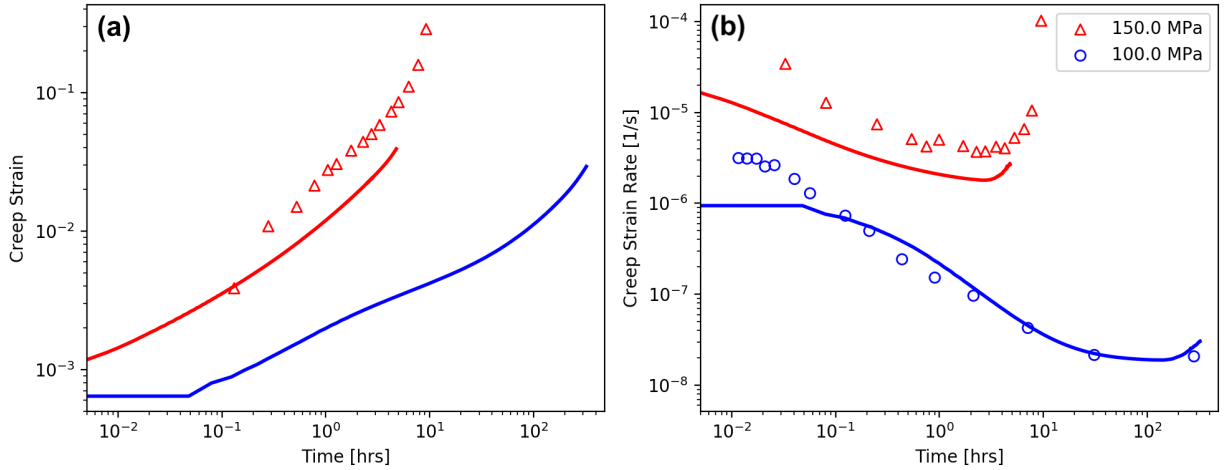

Figure 3: (a) Creep strain and (b) Creep rate for 923 K, open symbols represent the experimental data from (Shrestha et al., 2012; Basirat et al., 2012) and solid lines are from the numerical model.

with, by fitting against Basirat et al. experimental data, $\alpha_0 = 34.5$, $\alpha_T = 2.05 \times 10^4$, $\alpha_{T\Sigma} = 2.11 \times 10^4$, $\alpha_{T\Sigma^2} = -7.14 \times 10^3$.

Here, it should be pointed out that the search for a new lifetime predictor was not limited to any predetermined functional form. And so, it is interesting to note that the only differences from the Larson-Miller relation are in the higher order dependence on inverse temperature and isolated dependence on the logarithm of stress in Eq. 60. The large numerical database helps to determine the coefficients associated with these additional degrees of freedom.

In Figure 5(a), numerical and experimental data points from the creep rupture life database are presented by x's and filled circles, respectively, as a function of applied stress at different temperatures. The lifetime relation developed from numerical and experimental data is plotted by a solid line for each temperature, and the Larson-Miller lifetime relation, fit to experimental data, is plotted by the dashed lines.

The Larson-Miller relation fits the experimental data well, suggesting it is well-suited for interpolating among available short-term creep data. However, under longer lifetime conditions, extrapolations made using the Larson-Miller relation deviate from predictions made by the mechanistic CP/damage model. At the highest temperature, 973
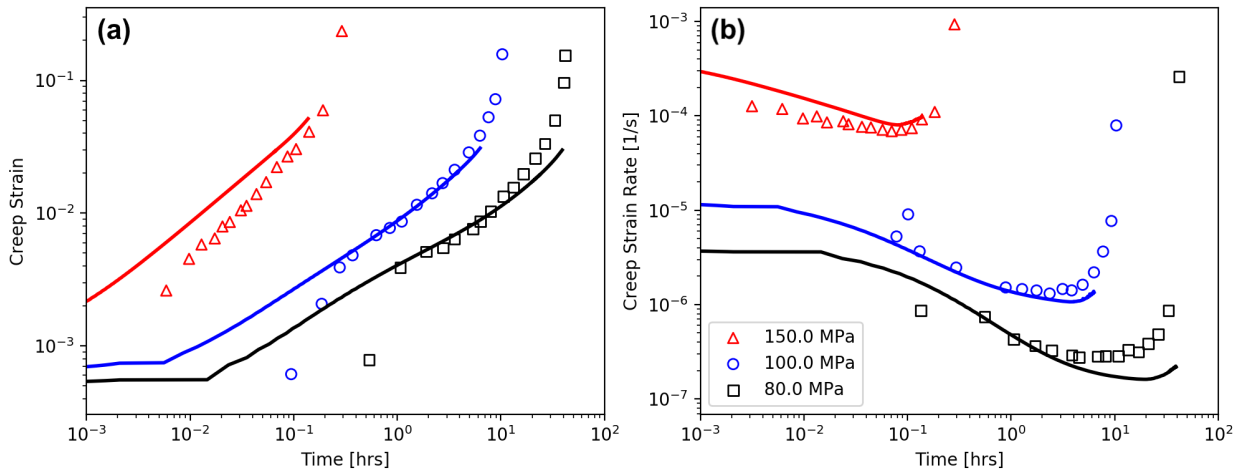
Figure 4: (a) Creep strain and (b) Creep rate for 973 K, open symbols represent the experimental data from (Shrestha et al., 2012; Basirat et al., 2012) and solid lines are from the numerical model.

K, the CP model predicts longer creep lifespans than the Larson-Miller relation, as stress is reduced. For example, at 30 MPa, the CP model predicts a creep rupture time of approximately 1000 hours, while the Larson-Miller relation predicts about 300 hours. At lower temperatures, the trend reverses and numerical observations of creep lifetime become much more conservative relative to the Larson-Miller relation. At 873 K and 100 MPa applied stress (just beyond the experimental dataset), the CP/damage model predicts a lifetime of approximately 9 months while the Larson-Miller relation predicts a lifetime greater than 3 years. At the lowest temperature and stress considered (873 K and 30 MPa), the numerical model predicts a lifespan of 4.5 years, while the Larson-Miller relation predicts a lifetime greater than 600 years. The more conservative predictions made by the numerical model suggest that a markedly different deformation mechanism has become significantly active at lower stresses and temperatures. This leads to lifetime trends that cannot be captured by fitting the Larson-Miller relation to experimental data from the high-stress regime. By contrast, these distinct deformation regimes are captured by fitting a new lifetime relation across the entire (numerical and experimental) creep lifetime database.

Variance in experimental data and uncertainty in the developed lifetime relation coefficients are quantified using a Bayesian framework, which are used to determine confidence intervals for the proposed lifespan relation. It is noted that no uncertainty in the parameters of the constitutive model was explicitly considered in these prediction intervals. The procedure for determining these prediction intervals is described in Appendix C.

These Bayesian uncertainty estimates inform middle 90-percentile prediction intervals for lifespan of Grade 91 steel, which are plotted by the shaded area in Figure 5(b) against applied stress at different temperatures. The Larson-Miller relation is again plotted by dashed lines. Even with 90% of the uncertainty distribution considered, the developed lifetime prediction intervals are several orders more conservative than the empirical Larson-Miller extrapolation procedure. As a final example, for one wishing to employ this Grade 91 steel under operating conditions of 873 K with an applied stress of 50 MPa, the model proposed herein indicates that 95% of the time the material will fail within 5 years. The Larson-Miller relation, however, predicts that the material should last over 200 years.

3.4. Further Improvements

The fidelity of any lifetime relation is conditioned upon the quality of the dataset it is trained on. In the current work, the CP-damage model predictions have been used to improve the overall creep lifetime dataset, by providing physically-justified observations under conditions that are too time-consuming to probe experimentally. However, in combining mechanistic mesoscale descriptions of plasticity and damage, this work also brings to light several shortcomings and inconsistencies among these fields, which may be used to motivate future work.

A homogenized model for simultaneous dissipation and void growth by point defect diffusion and viscoplastic processes does not currently exist. In the current work, independent descriptions for each process are summed from Eqs 50 and 51 to grow voids, and the effects on plasticity are summed in Eq. 1 from the formulations in Appendices A and B.
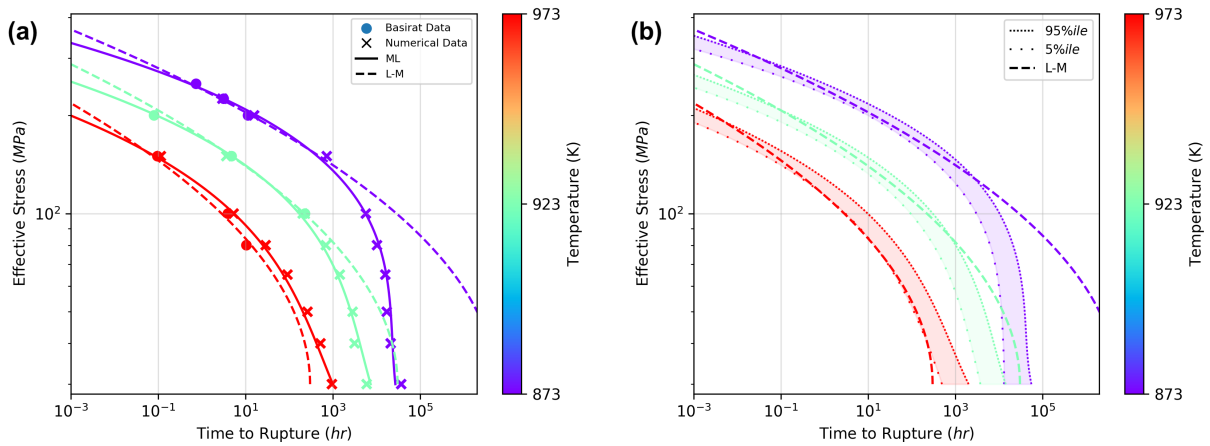
Figure 5: (a) Rupture life under applied stress and temperature, from experimental data from (Shrestha et al., 2012; Basirat et al., 2012) (filled circles), numerical model predictions ('x'), the deterministic form of the new lifetime relation (solid lines), and the Larson-Miller relation (dashed lines). (b) Confidence intervals for the new lifetime relation (represented by the shaded area) as compared to the Larson-Miller relation (dashed lines).

As discussed in (Wojtacki et al., 2020), the independent treatment of these processes can be considered a lower bound to their coupled effects, which might lead to much larger void growth rates and creep rates, especially in situations where diffusion and dislocation plasticity are highly active. These void evolution and dissipation models, from (Needleman and Rice, 1980; Leblond et al., 1994; Mbiakop et al., 2015), are each based on a unit cell description of void evolution. Since cavitation is often preferential at grain boundaries, a combined model should ideally consider a voided unit cell containing a grain boundary (or triple-junction or quadruple point) with anisotropic slip from dislocations in each grain as well as diffusive strain fields along grain interfaces. Such advanced damage model is currently not available, and it would require to be formulated in the future.

Currently, mesoscale predictions of void nucleation and coalescence rely on phenomenological models. To represent the former process in the current work, a distribution of critical void-nucleation strains is defined, following (Chu and Needleman, 1980). This is a natural choice for statistically modeling nucleation, but the distribution shape, variance, and mean can only be justified by fitting to the experimental creep and creep data. Similarly, the law in Eq. 58 only empirically accounts for void coalescence without explicitly describing the shape and orientation effects from coalesced voids. In-situ data on void number density, size, as well as shape and orientation statistics during creep would be of great value to parameterizing mesoscale creep damage models.

4. Conclusion

In this work, a physics-based constitutive law has been developed and exercised to model thermal creep and failure in Grade 91 steel. The model is based on the crystal plasticity law developed by (Wen et al., 2017), which explicitly describes dislocation climb and glide kinetics and dislocation content evolution at the material point level in the presence of relevant microstructure features. A relatively simple Arrhenius creep law is used to model diffusion-controlled plasticity.

A new damage law has been proposed, which models void distribution within each material point using a reaction-rate framework. Voids nucleate according to a strain-based criterion, and grow by coupled diffusion and viscoplastic processes. Local dislocation slip and diffusion are coupled with porosity using the anisotropic, crystallographic homogenization law from Mbiakop et al. (Mbiakop et al., 2015), and the isotropic homogenization law from Leblond et al. (Leblond et al., 1994), respectively.

The proposed constitutive law is implemented in a finite element framework to simulate uniaxial creep in a polycrystalline sample. Numerical results capture the stress and temperature sensitivities in Grade 91 steel, seen in short-term experiments from Basirat et al. (Basirat et al., 2012; Shrestha et al., 2012). The constitutive law was then exercised to simulate long-term creep at reduced stresses, and a large database of virtual experiments was generated.

A genetic programming module was trained against the database, and a new reduced-order lifetime predictor as a function of applied stress and temperature has been obtained. Uncertainties in lifetime predictions were quantified using a Bayesian framework, and used to develop prediction confidence intervals. When compared to typical lifespan predictors (which are empirically fit to short-term experimental data), the proposed lifetime assessment tool is shown to be several orders more conservative in lifespan prediction at lower temperatures and stresses.

This work illustrates a potential pathway for using physics-based, statistical models to redesign empirical lifetime relations. By describing the multiscale processes that are significant at various temperatures and stresses, physics-based models for plasticity and damage can harvest a large dataset that would experimentally take several decades.

Acknowledgements

Appendices

Appendix A: Effective Dissipation in Dislocation Slip due to Local Porosity

To account for the dissipative effects of local porosity on dislocation slip, the crystallographic homogenization model from Mbiakop et al. (Mbiakop et al., 2015) is used to define the resolved shear stress on each slip system in Eq. 5, with a modified variational compliance tensor $\mathbf{S}^{mvar}$:

$$\mathbf{S}^{mvar} = \mathbf{S}^{var} + (q_J^2 - 1)\mathbf{J} : \mathbf{S}^{var} : \mathbf{J} \tag{62}$$

In the above, $\mathbf{S}^{var}$ is the variational compliance tensor and q_J is a hydrostatic adjustment term that corrects overestimation of stiffness and captures material rate sensitivity, with the hydrostatic projection tensor $J_{ijkl} = \delta_{ij}\delta_{kl}/3$.

The hydrostatic adjustment term is:

$$q_J = \sqrt{\frac{15}{\bar{f}^*}} \left(\frac{(1 - \bar{f}^*)(\beta_n)^{1/n_{\mathrm{dis}}}}{n_{\mathrm{dis}}\left((\bar{f}^*)^{-1/n_{\mathrm{dis}}} - 1\right)} \right)^{n_{\mathrm{dis}}/(n_{\mathrm{dis}}+1)} \tag{63}$$

with

$$\beta_n = \frac{4}{25} 6^{-n_{\mathrm{dis}}/2} \tag{64}$$

where in (Mbiakop et al., 2015) plastic flow is described using a Norton-type power law with creep exponent n_{dis}.

The variational compliance tensor is computed using the estimate for a macro linear potential from Hashin-Shtrikman (Hashin and Shtrikman, 1963) and Willis (Willis, 1977):

$$\mathbf{S}^{var} = \frac{1}{2}\mathbf{M}^s + \frac{\bar{f}^*}{K}\mathbf{S}^* \tag{65}$$

where $\mathbf{M}^s$ is the fourth order Schmid projection tensor:

$$\mathbf{M}^s = 2(\mathbf{m}^s \otimes \mathbf{m}^s) \tag{66}$$

and $\mathbf{S}^*$ (and $\mathbf{Q}$) are fourth order microstructure tensors:

$$\mathbf{S}^* = \mathbf{Q}^{-1} - \sum_s^K \frac{1}{2}\mathbf{M}^s \tag{67}$$

$$\mathbf{Q} = \lim_{\hat{\rho} \to \infty} \lim_{\hat{\kappa} \to \infty} \left[\mathbf{S}^{-1} - \mathbf{S}^{-1} : \mathbf{P} : \mathbf{S}^{-1} \right] \tag{68}$$

$\mathbf{P}$ is the Eshelby tensor (Willis, 1977) (in this case for a spherical void):

$$P_{ijkl} = \frac{1}{4\pi} \int_{|\xi|=1} \mathbf{L}_{ik}^{-1} \xi_j \xi_l \, dS \tag{69}$$

where ξ is a unit vector and $L_{ij} = \mathbf{S}_{iajb}^{-1} \xi_a \xi_b$. $\mathbf{S}$ is the linear compliance tensor:

$$\mathbf{S} = \sum_s^K \frac{1}{2} \mathbf{M}^s + \frac{1}{2\hat{\rho}} \sum_s^K \mathbf{F}^s + \frac{1}{3\hat{\kappa}} \mathbf{J} \tag{70}$$

with $\mathbf{F}^s = \mathbf{K} - \mathbf{M}^s$, where $\mathbf{K}$ is the fourth order deviatoric projection tensor, $K_{ijkl} = I_{ijkl} - J_{ijkl}$ with $I_{ijkl} = (\delta_{ik}\delta_{jl} + \delta_{il}\delta_{jk})/2$.

The term $\hat{\rho}$ is the normalized modulus perpendicular to slip, and is taken to infinity since no slip occurs in that direction. The normalized bulk modulus, $\hat{\kappa}$, is also taken to infinity for an incompressible material. In the formulation from (Mbiakop et al., 2015), these moduli are normalized by a linear comparison composite modulus, which is assumed equal on each slip system. This assumption is valid in the current work since the critical resolved shear stress was never seen to vary by more than 5% among slip systems.

Appendix B: Effective Dissipation in Point Defect Diffusion due to Local Porosity

The isotropic homogenization law from Leblond et al. (Leblond et al., 1994) is used to capture the dissipative effects of porosity on point defect transport. Specifically, the local equivalent stress used in Eq. 36 is defined as a function of local von Mises stress and porosity, by implicitly setting the yield surface from (Leblond et al., 1994) equal to zero:

$$\Phi = \left(\frac{\sigma_{eq}}{\tilde{\sigma}_{eq}} \right)^2 + 2q_1 \bar{f}^* \left[H_n \left(\frac{\sigma_m}{\tilde{\sigma}_{eq}} \right) + \frac{n_{\text{diff}} - 1}{n_{\text{diff}} + 1} \frac{1}{H_n \left(\frac{\sigma_m}{\tilde{\sigma}_{eq}} \right)} \right] - 1 - \frac{n_{\text{diff}} - 1}{n_{\text{diff}} + 1} \left(q_1 \bar{f}^* \right)^2 = 0 \tag{71}$$

In the above, σ_{eq} is the local von Mises stress and n_{diff} is the creep exponent. In the case of approximately spherical voids, the hydrostatic rate-sensitivity adjustment function, H_n, is given by:

$$H_n(x) = \left[1 + \frac{1}{n_{\text{diff}}} \left(\frac{3q_2|x|}{2} \right)^{(n_{\text{diff}}+1)/n_{\text{diff}}} \right]^{1/n_{\text{diff}}} \tag{72}$$

with damage parameters q_1 and q_2.

Appendix C: Bayesian Framework

A Bayesian framework (Tiao and Zellner, 1964; Gelman et al., 2013) is employed to account for the experimental data and the numerical data in different ways in determining the expected variability and parameter uncertainty of the different lifetime predictions. The lifetime prediction equations are treated using ordinary linear least-squares regression of the Basirat data:

$$\mathbf{y} \big| \boldsymbol{\beta}, \sigma, \mathbf{X} \sim N(\mathbf{X}\boldsymbol{\beta}, \sigma^2) \tag{73}$$

where $N(m, s)$ denotes a normal distribution with mean m and variance s, $\boldsymbol{\beta}$ is a vector of the coefficients $(\alpha_\Sigma, \alpha_T, ...)$ of the terms in the lifetime prediction equation in Eq 60, and σ is the standard deviation in the Basirat data. The observations of time to rupture are shown as vector $\mathbf{y}$ and the associated values of temperature and stress are shown as matrix $\mathbf{X}$. Prior probability is assigned to the standard deviation as,

$$p\left(\boldsymbol{\beta}, \sigma^2 \big| \mathbf{X} \right) \propto \sigma^{-2} \tag{74}$$

The linear least squares estimate of $\boldsymbol{\beta}$, shown as $\hat{\boldsymbol{\beta}}$, is given in the common form,

$$\hat{\boldsymbol{\beta}} = (\mathbf{X}^T\mathbf{X})^{-1}\mathbf{X}^T\mathbf{y} \tag{75}$$

and the covariance matrix of the parameter estimates $\mathbf{V}_{\boldsymbol{\beta}}$ is given as,

$$\mathbf{V}_{\boldsymbol{\beta}} = (\mathbf{X}^T\mathbf{X})^{-1} \tag{76}$$

As mentioned, the experiments and numerical simulations are used together to inform the lifetime predictions. While the physics-based model allows the numerical simulations to inform the estimation of the parameters in the lifetime equation, the variance of the experimental data is not replicated by the numerical simulations gathered here. As such, the estimation of the parameters $\boldsymbol{\beta}$ are based on both experiments and numerical simulations, while the overall population variance σ^2 should only reflect experimental data. An estimate of population variance can be determined from the variance in the available experimental samples, i.e. sample variance s^2, by:

$$\sigma^2\big|\mathbf{y} \sim \mathrm{Inv}\chi^2(n_{\mathrm{exp}} - k, s^2) \tag{77}$$

where n_{exp} is number of experimental observations, and k is the number of coefficients in the model, and $\mathrm{Inv}\chi^2$ refers to the inverse chi-squared probability distribution with $n_{\mathrm{exp}} - k$ degrees of freedom and sample variance s^2. Variance in the sample data is calculated by,

$$s^2 = \frac{1}{n_{\mathrm{exp}} - k}(\mathbf{y}_{\mathrm{exp}} - \mathbf{X}_{\mathrm{exp}}\hat{\boldsymbol{\beta}})^T(\mathbf{y}_{\mathrm{exp}} - \mathbf{X}_{\mathrm{exp}}\hat{\boldsymbol{\beta}}) \tag{78}$$

where subscript 'exp' denotes that only the Basirat data is included. Notably, the estimate of $\boldsymbol{\beta}$ in this equation is based on numerical and experimental data.

Prediction intervals are used to project a range of lifetimes to expect at a prescribed temperature and applied effective stress, $\tilde{\mathbf{X}}$. The values of these can be calculated from the prediction probability distribution,

$$\tilde{\mathbf{y}} \sim \mathrm{T}_{n_{\mathrm{exp}}-k}\big(\tilde{\mathbf{X}}\hat{\boldsymbol{\beta}}, s^2(\mathbf{I} + \tilde{\mathbf{X}}\mathbf{V}_{\boldsymbol{\beta}}\tilde{\mathbf{X}}^T)\big) \tag{79}$$

which is a multivariate-t distribution with $n_{\mathrm{exp}}-k$ degrees of freedom, center $\tilde{\mathbf{X}}\hat{\boldsymbol{\beta}}$, and scale matrix $s^2(\mathbf{I}+\tilde{\mathbf{X}}\mathbf{V}_{\boldsymbol{\beta}}\tilde{\mathbf{X}}^T)$. The scale matrix contains the variability observed in the experimental data as well as uncertainty in parameter estimates as $\tilde{\mathbf{X}}$ deviates from $\mathbf{X}$.

CRediT authorship contribution statement

References

Abe, F., 2008. Precipitate design for creep strengthening of 9% cr tempered martensitic steel for ultra-supercritical power plants. Science and Technology of advanced materials 9, 013002.

Ashby, M., 1983. Mechanisms of deformation and fracture, Elsevier. volume 23 of *Advances in Applied Mechanics*, pp. 117 – 177. URL: http://www.sciencedirect.com/science/article/pii/S0065215608702436, doi:https://doi.org/10.1016/S0065-2156(08)70243-6.

Austin, R.A., McDowell, D.L., 2011. A dislocation-based constitutive model for viscoplastic deformation of fcc metals at very high strain rates. International Journal of Plasticity 27, 1–24.

Bakó, B., Clouet, E., Dupuy, L.M., Blétry, M., 2011. Dislocation dynamics simulations with climb: kinetics of dislocation loop coarsening controlled by bulk diffusion. Philosophical Magazine 91, 3173–3191.

Basirat, M., Shrestha, T., Potirniche, G., Charit, I., Rink, K., 2012. A study of the creep behavior of modified 9cr–1mo steel using continuum-damage modeling. International Journal of Plasticity 37, 95 – 107. URL: http://www.sciencedirect.com/science/article/pii/S0749641912000678, doi:https://doi.org/10.1016/j.ijplas.2012.04.004.

Bertin, N., Tomé, C., Beyerlein, I., Barnett, M., Capolungo, L., 2014. On the strength of dislocation interactions and their effect on latent hardening in pure magnesium. International Journal of Plasticity 62, 72 – 92. URL: http://www.sciencedirect.com/science/article/pii/S0749641914001326, doi:https://doi.org/10.1016/j.ijplas.2014.06.010.

Besson, J., 2009. Damage of ductile materials deforming under multiple plastic or viscoplastic mechanisms. International Journal of Plasticity 25, 2204 – 2221. URL: http://www.sciencedirect.com/science/article/pii/S0749641909000357, doi:https://doi.org/10.1016/j.ijplas.2009.03.001.

Cerri, E., Evangelista, E., Spigarelli, S., Bianchi, P., 1998. Evolution of microstructure in a modified 9cr–1mo steel during short term creep. Materials Science and Engineering: A 245, 285–292.

Chu, C., Needleman, A., 1980. Void nucleation effects in biaxially stretched sheets. Journal of engineering materials and technology 102, 249–256.

Chuang, T.J., Kagawa, K.I., Rice, J.R., Sills, L.B., 1979. Overview no. 2: Non-equilibrium models for diffusive cavitation of grain interfaces. Acta Metallurgica 27, 265 – 284. URL: http://www.sciencedirect.com/science/article/pii/000161607990021X, doi:https://doi.org/10.1016/0001-6160(79)90021-X.

Clifton, R., 1971. Shock waves and the mechanical properties of solids, in: Proceedings of the 17th Sagamore Army Materials Research Conference. Sagamore Conference Center, Raquette Lake, NY September 1–4, 1970, Syracuse University Press NY. p. 73.

Dong, Y., Nogaret, T., Curtin, W., 2010. Scaling of dislocation strengthening by multiple obstacle types. Metallurgical and Materials Transactions A 41, 1954–1960.

Estrin, Y., 1998. Dislocation theory based constitutive modelling: foundations and applications. Journal of Materials Processing Technology 80-81, 33 – 39. URL: http://www.sciencedirect.com/science/article/pii/S0924013698002088, doi:https://doi.org/10.1016/S0924-0136(98)00208-8.

Feng, L., shi Zhang, K., Zhang, G., dong Yu, H., 2002. Anisotropic damage model under continuum slip crystal plasticity theory for single crystals. International Journal of Solids and Structures 39, 5279 – 5293. URL: http://www.sciencedirect.com/science/article/pii/S0020768302004092, doi:https://doi.org/10.1016/S0020-7683(02)00409-2.

Field, K.G., Hu, X., Littrell, K.C., Yamamoto, Y., Snead, L.L., 2015. Radiation tolerance of neutron-irradiated model fe–cr–al alloys. Journal of Nuclear Materials 465, 746–755.

Foldyna, V., Kubon, Z., Filip, M., Mayer, K.H., Berger, C., 1996. Evaluation of structural stability and creep resistance of 9-12% cr steels. steel research 67, 375–381.

Franciosi, P., Zaoui, A., 1982. Multislip in f.c.c. crystals a theoretical approach compared with experimental data. Acta Metallurgica 30, 1627 – 1637. URL: http://www.sciencedirect.com/science/article/pii/0001616082901845, doi:https://doi.org/10.1016/0001-6160(82)90184-5.

Gaffard, V., 2004. Experimental study and modeling of behavior, damage and high-temperature creep rupture of 9cr1Mo-NbVS steel welded joints. Ph.D. thesis. URL: http://www.theses.fr/2004ENMP1269. doctoral Thesis directed by Besson, Jacques Sciences and Materials Engineering Paris, ENMP 2004.

Gaffard, V., Besson, J., Gourgues-Lorenzon, A.F., 2005. Creep failure model of a tempered martensitic stainless steel integrating multiple deformation and damage mechanisms. International Journal of Fracture 133, 139–166. URL: https://doi.org/10.1007/s10704-005-2528-8, doi:10.1007/s10704-005-2528-8.

Geers, M., Cottura, M., Appolaire, B., Busso, E.P., Forest, S., Villani, A., 2014. Coupled glide-climb diffusion-enhanced crystal plasticity. Journal of the Mechanics and Physics of Solids 70, 136–153.

Gelman, A., Carlin, J., Stern, H., Dunson, D., Vehtari, A., Rubin, D., 2013. Bayesian Data Analysis. Chapman & Hall/CRC Texts in Statistical Science, CRC Press. URL: https://books.google.com/books?id=eSHSBQAAQBAJ.

Granato, A., Lücke, K., Schlipf, J., Teutonico, L., 1964. Entropy factors for thermally activated unpinning of dislocations. Journal of Applied Physics 35, 2732–2745.

Gu, Y., Xiang, Y., Quek, S.S., Srolovitz, D.J., 2015. Three-dimensional formulation of dislocation climb. Journal of the Mechanics and Physics of Solids 83, 319 – 337. URL: http://www.sciencedirect.com/science/article/pii/S0022509615000691, doi:https://doi.org/10.1016/j.jmps.2015.04.002.

Gurson, A.L., 1977. Continuum theory of ductile rupture by void nucleation and growth: Part i—yield criteria and flow rules for porous ductile media. Journal of engineering materials and technology 99, 2–15.

Hald, J., 2008. Microstructure and long-term creep properties of 9–12% cr steels. International Journal of Pressure Vessels and Piping 85, 30–37.

Hartley, C., 2003. A method for linking thermally activated dislocation mechanisms of yielding with continuum plasticity theory. Philosophical Magazine 83, 3783–3808. URL: https://doi.org/10.1080/14786430310001599522, doi:10.1080/14786430310001599522, arXiv:https://doi.org/10.1080/14786430310001599522.

Hashin, Z., Shtrikman, S., 1963. A variational approach to the theory of the elastic behaviour of multiphase materials. Journal of the Mechanics and Physics of Solids 11, 127–140.

Hayakawa, H., Nakashima, S., Kusumoto, J., Kanaya, A., Nakashima, H., 2009. Creep deformation characterization of heat resistant steel by stress change test. International Journal of Pressure Vessels and Piping 86, 556–562.

Hecht, F., 2012. New development in freefem++. J. Numer. Math. 20, 251–265. URL: https://freefem.org/.

Hirth, J.P., Lothe, J., Mura, T., 1983. Theory of dislocations. Journal of Applied Mechanics 50, 476.

Hull, D., Rimmer, D., 1959. The growth of grain-boundary voids under stress. Philosophical Magazine 4, 673–687.

Kim, J.B., Yoon, J.W., 2015. Necking behavior of aa 6022-t4 based on the crystal plasticity and damage models. International Journal of Plasticity 73, 3 – 23. URL: http://www.sciencedirect.com/science/article/pii/S0749641915001096, doi:https://doi.org/10.1016/j.ijplas.2015.06.013. special Issue on Constitutive Modeling from Micro-Scale to Continuum in Honor of Prof. Frédéric Barlat.

Kimura, K., Sawada, K., Kushima, H., Toda, Y., 2013. Influence of chemical composition and heat treatment on long-term creep strength of grade 91 steel. Procedia Engineering 55, 2 – 9. URL: http://www.sciencedirect.com/science/article/pii/S1877705813005651, doi:https://doi.org/10.1016/j.proeng.2013.03.211. 6th International Conference on Creep, Fatigue and Creep-Fatigue Interaction.

Kocks, U., Argon, A., Ashby, M., 1975. Thermodynamics and Kinetics of Slip. Progress in materials science, Pergamon Press. URL: https://books.google.com/books?id=BOAkMgEACAAJ.

Lagerpusch, U., Mohles, V., Baither, D., Anczykowski, B., Nembach, E., 2000. Double strengthening of copper by dissolved gold-atoms and by incoherent sio2-particles: how do the two strengthening contributions superimpose? Acta materialia 48, 3647–3656.

Larson, F.R., 1952. A time-temperature relationship for rupture and creep stresses. Trans. ASME 74, 765–775.

Lebensohn, R., Tomé, C., 1993. A self-consistent anisotropic approach for the simulation of plastic deformation and texture development of polycrystals: Application to zirconium alloys. Acta Metallurgica et Materialia 41, 2611 – 2624. URL: http://www.sciencedirect.com/science/article/pii/095671519390130K, doi:https://doi.org/10.1016/0956-7151(93)90130-K.

Lebensohn, R.A., Hartley, C.S., Tomé, C.N., Castelnau, O., 2010. Modeling the mechanical response of polycrystals deforming by climb and glide. Philosophical Magazine 90, 567–583. URL: https://doi.org/10.1080/14786430903213320, doi:10.1080/14786430903213320, arXiv:https://doi.org/10.1080/14786430903213320.

Leblond, J., Perrin, G., Suquet, P., 1994. Exact results and approximate models for porous viscoplastic solids. International Journal of Plasticity 10, 213 – 235. URL: http://www.sciencedirect.com/science/article/pii/0749641994900019, doi:https://doi.org/10.1016/0749-6419(94)90001-9.

Lloyd, J., Clayton, J., Austin, R., McDowell, D., 2014. Plane wave simulation of elastic-viscoplastic single crystals. Journal of the Mechanics and Physics of Solids 69, 14 – 32. URL: http://www.sciencedirect.com/science/article/pii/S0022509614000775, doi:https://doi.org/10.1016/j.jmps.2014.04.009.

Maruyama, K., Sawada, K., Koike, J.i., 2001. Strengthening mechanisms of creep resistant tempered martensitic steel. ISIJ international 41, 641–653.

Mbiakop, A., Constantinescu, A., Danas, K., 2015. An analytical model for porous single crystals with ellipsoidal voids. Journal of the Mechanics and Physics of Solids 84, 436 – 467. URL: http://www.sciencedirect.com/science/article/pii/S002250961530017X, doi:https://doi.org/10.1016/j.jmps.2015.07.011.

Mendelev, M.I., Mishin, Y., 2009. Molecular dynamics study of self-diffusion in bcc fe. Physical review B 80, 144111.

Mendelson, A., Ernest, Jr, R., Manson, S., 1965. Optimization of time-temperature parameters for creep and stress rupture, with application to data from german cooperative long-time creep program , 37.

Monkman, F., Grant, N., 1956. American society of testing materials, in: Proceedings, pp. 593–620.

Murchú, C., Leen, S., O'Donoghue, P., Barrett, R., 2017. A physically-based creep damage model for effects of different precipitate types. Materials Science and Engineering: A 682, 714 – 722. URL: http://www.sciencedirect.com/science/article/pii/S0921509316313983, doi:https://doi.org/10.1016/j.msea.2016.11.044.

Nakajima, T., Spigarelli, S., Evangelista, E., Endo, T., 2003. Strain enhanced growth of precipitates during creep of t91. Materials Transactions 44, 1802–1808.

Needleman, A., Rice, J., 1980. Plastic creep flow effects in the diffusive cavitation of grain boundaries. Acta Metallurgica 28, 1315 – 1332. URL: http://www.sciencedirect.com/science/article/pii/0001616080900012, doi:https://doi.org/10.1016/0001-6160(80)90001-2.

Nes, E., 1997. Modelling of work hardening and stress saturation in fcc metals. Progress in Materials Science 41, 129 – 193. URL: http://www.sciencedirect.com/science/article/pii/S0079642597000327, doi:https://doi.org/10.1016/S0079-6425(97)00032-7.

Orr, R.L., Sherby, O.D., Dorn, J.E., 1953. Correlations of rupture data for metals at elevated temperatures. Technical Report. Institue of Engineering Research, Univ. of Calif., Berkeley.

Pandey, C., Mahapatra, M.M., Kumar, P., Saini, N., 2018. Some studies on p91 steel and their weldments. Journal of Alloys and Compounds 743, 332 – 364. URL: http://www.sciencedirect.com/science/article/pii/S092583881830121X, doi:https://doi.org/10.1016/j.jallcom.2018.01.120.

Patra, A., McDowell, D.L., 2012. Crystal plasticity-based constitutive modelling of irradiated bcc structures. Philosophical Magazine 92, 861–887. URL: https://doi.org/10.1080/14786435.2011.634855, doi:10.1080/14786435.2011.634855, arXiv:https://doi.org/10.1080/14786435.2011.634855.

Potirniche, G., Horstemeyer, M., Ling, X., 2007. An internal state variable damage model in crystal plasticity. Mechanics of Materials 39, 941 – 952. URL: http://www.sciencedirect.com/science/article/pii/S0167663607000592, doi:https://doi.org/10.1016/j.mechmat.2007.04.004.

Queyreau, S., Monnet, G., Devincre, B., 2009. Slip systems interactions in α-iron determined by dislocation dynamics simulations. International Journal of Plasticity 25, 361–377.

Roters, F., Eisenlohr, P., Hantcherli, L., Tjahjanto, D., Bieler, T., Raabe, D., 2010. Overview of constitutive laws, kinematics, homogenization and multiscale methods in crystal plasticity finite-element modeling: Theory, experiments, applications. Acta Materialia 58, 1152 – 1211. URL: http://www.sciencedirect.com/science/article/pii/S1359645409007617, doi:https://doi.org/10.1016/j.actamat.2009.10.058.

Sawada, K., Miyahara, K., Kushima, H., Kimura, K., Matsuoka, S., 2005. Contribution of microstructural factors to hardness change during creep exposure in mod.9cr-1mo steel. ISIJ International 45, 1934–1939. doi:10.2355/isijinternational.45.1934.

Sham, T.L., Needleman, A., 1983. Effects of triaxial stressing on creep cavitation of grain boundaries. Acta Metallurgica 31, 919–926.

Shrestha, T., Basirat, M., Charit, I., Potirniche, G.P., Rink, K.K., 2013. Creep rupture behavior of grade 91 steel. Materials Science and Engineering: A 565, 382 – 391. URL: http://www.sciencedirect.com/science/article/pii/S0921509312017194, doi:https://doi.org/10.1016/j.msea.2012.12.031.

Shrestha, T., Basirat, M., Charit, I., Potirniche, G.P., Rink, K.K., Sahaym, U., 2012. Creep deformation mechanisms in modified 9cr–1mo steel. Journal of Nuclear Materials 423, 110 – 119. URL: http://www.sciencedirect.com/science/article/pii/S0022311512000098, doi:https://doi.org/10.1016/j.jnucmat.2012.01.005.

Sills, R.B., Boyce, B., 2020. Void growth by dislocation adsorption. Materials Research Letters 8, 103–109.

Sobie, C., Bertin, N., Capolungo, L., 2015. Analysis of obstacle hardening models using dislocation dynamics: application to irradiation-induced defects. Metallurgical and Materials Transactions A 46, 3761–3772.

Spigarelli, S., Cerri, E., Bianchi, P., Evangelista, E., 1999. Interpretation of creep behaviour of a 9cr–mo–nb–v–n (t91) steel using threshold stress concept. Materials Science and Technology 15, 1433–1440. URL: https://doi.org/10.1179/026708399101505428, doi:10.1179/026708399101505428, arXiv:https://doi.org/10.1179/026708399101505428.

Stephens, T., 2019. Genetic programming in python, with scikit-learn inspired api. URL: https://gplearn.readthedocs.io/en/stable/.

Tiao, G.C., Zellner, A., 1964. On the bayesian estimation of multivariate regression. Journal of the Royal Statistical Society: Series B (Methodological) 26, 277–285. URL: https://rss.onlinelibrary.wiley.com/doi/abs/10.1111/j.2517-6161.1964.tb00560.x, doi:https://doi.org/10.1111/j.2517-6161.1964.tb00560.x, arXiv:https://rss.onlinelibrary.wiley.com/doi/pdf/10.1111/j.2517-6161.1964.tb00560.x.

Tvergaard, V., Needleman, A., 1984. Analysis of the cup-cone fracture in a round tensile bar. Acta metallurgica 32, 157–169.

Van Der Giessen, E., Van der Burg, M., Needleman, A., Tvergaard, V., 1995. Void growth due to creep and grain boundary diffusion at high triaxialities. Journal of the Mechanics and Physics of Solids 43, 123–165.

Wang, H., Capolungo, L., Clausen, B., Tomé, C., 2017. A crystal plasticity model based on transition state theory. International Journal of Plasticity 93, 251 – 268. URL: http://www.sciencedirect.com/science/article/pii/S0749641916300717, doi:https://doi.org/10.1016/j.ijplas.2016.05.003. special Issue on Constitutive Descriptions of Plasticity atVarious Scales in memory of Prof. José J. Grácio.

Wang, H., Clausen, B., Capolungo, L., Beyerlein, I.J., Wang, J., Tome, C.N., 2016. Stress and strain relaxation in magnesium az31 rolled plate: In-situ neutron measurement and elastic viscoplastic polycrystal modeling. International Journal of Plasticity 79, 275–292.

Was, G.S., 2016. Fundamentals of radiation materials science: metals and alloys. Springer.

Wen, W., Capolungo, L., Patra, A., Tomé, C.N., 2017. A physics-based crystallographic modeling framework for describing the thermal creep behavior of fe-cr alloys. Metallurgical and Materials Transactions A 48, 2603–2617. URL: https://doi.org/10.1007/s11661-017-4011-3, doi:10.1007/s11661-017-4011-3.

Wen, W., Kohnert, A., Arul Kumar, M., Capolungo, L., Tomé, C., 2020. Mechanism-based modeling of thermal and irradiation creep behavior: An application to ferritic/martensitic ht9 steel. International Journal of Plasticity 126, 102633. URL: http://www.sciencedirect.com/science/article/pii/S0749641919305868, doi:https://doi.org/10.1016/j.ijplas.2019.11.012.

Whittaker, M.T., Harrison, W.J., 2014. Evolution of wilshire equations for creep life prediction. Materials at High Temperatures 31, 233–238. URL: https://doi.org/10.1179/1878641314Y.0000000019, doi:10.1179/1878641314Y.0000000019, arXiv:https://doi.org/10.1179/1878641314Y.0000000019.

Willis, J., 1977. Bounds and self-consistent estimates for the overall properties of anisotropic composites. Journal of the Mechanics and Physics of Solids 25, 185–202.

Wilshire, B., Battenbough, A.J., 2007. Creep and creep fracture of polycrystalline copper. Materials Science and Engineering A-Structural Materials Properties Microstructure and Processing 443, 156–166. doi:{10.1016/j.msea.2006.08.094}.

Wojtacki, K., Vincent, P.G., Suquet, P., Moulinec, H., Boittin, G., 2020. A micromechanical model for the secondary creep of elasto-viscoplastic porous materials with two rate-sensitivity exponents: Application to a mixed oxide fuel. International Journal of Solids and Structures 184, 99 – 113. URL: http://www.sciencedirect.com/science/article/pii/S0020768318305237, doi:https://doi.org/10.1016/j.ijsolstr.2018.12.026. physics and Mechanics of Random Structures: From Morphology to Material Properties.

Yadav, S.D., Kalácska, S., Dománková, M., Yubero, D.C., Resel, R., Groma, I., Beal, C., Sonderegger, B., Sommitsch, C., Poletti, C., 2016. Evolution of the substructure of a novel 12% cr steel under creep conditions. Materials characterization 115, 23–31.

Yamamoto, Y., Pint, B.A., Terrani, K.A., Field, K.G., Yang, Y., Snead, L.L., 2015. Development and property evaluation of nuclear grade wrought fecral fuel cladding for light water reactors. Journal of Nuclear Materials 467, 703–716.

Zhao, N., Roy, A., Wang, W., Zhao, L., Silberschmidt, V.V., 2019. Coupling crystal plasticity and continuum damage mechanics for creep assessment in cr-based power-plant steel. Mechanics of Materials 130, 29 – 38. URL: http://www.sciencedirect.com/science/article/pii/S0167663618305192, doi:https://doi.org/10.1016/j.mechmat.2019.01.006.